J Mater Sci (2008) 43:7026–7034
DOI 10.1007/s10853-008-3034-y

Preparation, characterization and photocatalytic properties of nanoplate Bi_2MoO_6 catalysts

HongHua Li · ChaoYu Liu · KunWei Li · Hao Wang

Received: 7 July 2008 / Accepted: 3 October 2008 / Published online: 30 October 2008

Abstract Bismuth molybdate (Bi_2MoO_6) nanoplates have been successfully synthesized by a simple hydrothermal process. The nanoplates were characterized by X-ray diffraction (XRD), scanning electron microscopy (SEM), transmission electron microscopy (TEM), Raman spectroscopy, and IR spectroscopy. The effects of hydrothermal temperature and reaction time on the structures and morphologies of the nanoplates were investigated. On the basis of TEM observation of time series samples, a possible formation mechanism of the nanoplates was proposed. Optical absorption experiments revealed that Bi_2MoO_6 nanoplates had absorption in visible-light region, but a blue shift appeared compared with the corresponding bulk materials. Photocatalytic experiments showed that the nanoplates exhibited good photocatalytic activities for degradation of *N*,*N*,*N*′,*N*′-tetraethylated rhodamine (RhB) under visible-light irradiation ($\lambda > 420$ nm).

Introduction

Photocatalysis using solar energy and semiconductors is of importance in solving global energy and environment issues. Great progress has been made in the research and application for this field since photoelectrochemical water splitting (the Honda–Fujishima effect) was reported in 1972 [1, 2]. However, most of the photocatalysts developed thus far have wide bandgaps, and merely absorb UV light, which unfortunately results in limited practical application, since the solar spectrum contains only ca. 4% of UV light. Visible light is far more abundant (ca. 46%) and thus a more useful region in the solar spectrum, whereas only a few photocatalysts driven by visible light have been discovered so far [3–6]. Therefore, developing visible-light-responsive photocatalysts is still a challenge at the present time.

Aurivillius oxides with general formula $Bi_2A_{n-1}B_nO_{3n+3}$ (A = Ca, Sr, Ba, Pb, Na, K, and B = Ti, Nb, Ta, Mo, W, Fe) have gained much attention due to their layer structure and unique properties [7–10]. Bi_2MoO_6 is one of the simplest members of the Aurivillius oxide family when $n = 1$ [11, 12]. In addition, Bi_2MoO_6 possesses many interesting and important physical and chemical properties such as ion conducting [13, 14], dielectric properties [15], gas sensor [16], and catalytic behavior [17–19]. Lately, Bi_2MoO_6 showed photocatalytic activities under visible-light irradiation. For example, Kudo et al. [20, 21] fabricated Bi_2MoO_6 by hydrothermal and reflux methods, respectively, and investigated its visible-light-driven photocatalytic activity for O_2 evolution from an aqueous $AgNO_3$ solution. Bi, Xie, and Cruz et al. [22–24] synthesized Bi_2MoO_6 by solvothermal, molten salt, and complex organic precursor methods, respectively, and revealed that Bi_2MoO_6 could degrade Rhodamine B under visible-light irradiation. Zhao et al. [25] investigated the photocatalytic activity of Bi_2MoO_6 film toward the degradation of Azo dyes under visible-light irradiation. However, to the best of our knowledge, there is little systemic study on visible-light photocatalytic activity of Bi_2MoO_6 prepared by hydrothermal method toward the degradation of organic contaminants.

In this paper, Bi_2MoO_6 nanoplates have been synthesized by a simple surfactant-free hydrothermal approach. The nanoplates were characterized by X-ray diffraction (XRD), scanning electron microscopy (SEM), transmission

H. Li · C. Liu · K. Li · H. Wang (✉)
The College of Materials Science and Engineering, Beijing University of Technology, Beijing 100022, China
e-mail: haowang@bjut.edu.cn

electron microscopy (TEM), Raman spectroscopy, and IR spectroscopy. The effects of hydrothermal temperature and reaction time on the structures and morphologies of the nanoplates were systemically investigated. Photocatalytic degradation for RhB under visible-light irradiation was used to investigate the photocatalytic performance of the synthesized nanoplates. The results show that Bi_2MoO_6 nanoplates have high photocatalytic activity under visible-light irradiation and that crystallinity and defects in Bi_2MoO_6 crystals are the predominant factors affecting photocatalytic activity.

Experimental section

Synthesis

All chemicals were of analytical grade and were used without further purification. In a typical synthesis, 5.0 mmol of $Bi(NO_3)_3 \cdot 5H_2O$ and 2.5 mmol H_2MoO_4 were dissolved in deionized water. Then, 0.2 M NaOH solution was added to the above solution with magnetic stirring. The mixture was stirred for 0.5 h. This precursor solution was poured into a Teflon-lined stainless steel autoclave until 80% of the volume of the autoclave was occupied. After that, the autoclave was sealed into a stainless steel tank and kept at series experiment conditions. All temperature series samples were treated from 100 °C to 240 °C for 24 h, while all time series samples were prepared at 180 °C for different hours. Then the reactor was cooled to room temperature naturally. Resulting samples were collected and washed with deionized water and dried at 80 °C in air. Meanwhile Bi_2MoO_6 were synthesized by traditional solid-state reaction for comparison with the nanoplates.

Characterization

Crystallographic phases and purity information of the prepared samples were investigated by X-ray diffraction at room temperature with a Bruker AXS D8 ADVANCE diffractometer using CuKα1 radiation ($\lambda = 1.5405$ Å). The morphology and microstructure of the products were determined by transmission electron microscopy (TEM H8100) with an accelerating voltage of 200 kV. Raman spectra were obtained on a Britain Renishaw Invia Raman spectrometer with a solid-state laser (excitation at 785 nm) at room temperature in the range of 200–800 cm^{-1}. FT-IR spectra were recorded on a Perkin-Elmer Spectrum One FT-IR machine at wavenumbers 400–4000 cm^{-1} by using KBr for diluting (sample: KBr = 0.5:100). Shimadzu UV-3101PC ultraviolet–visible–near infrared (UV–vis–NIR) spectrophotometer was used to investigate the optical absorption of powder and solution. UV–visible absorption spectra of powder samples were recorded using pure $BaSO_4$ pellet as the reference.

Photocatalytic test

The photocatalytic activity of the Bi_2MoO_6 nanoplates was evaluated by degradation of RhodamineB under visible-light irradiation of a 500 W Xe lamp with a 420 nm cutoff filter. The reaction cell was wrapped by tinfoil and the cutoff filter was placed on the top to provide visible-light irradiation. In each experiment, 0.05 g of photocatalysts without cocatalyst were added into 100 mL Rhodamine-B solution (1×10^{-5} M). Prior to irradiation, the suspensions were magnetically stirred in the dark for 15 min to establish adsorption/desorption equilibrium. The suspensions were then exposed to visible-light irradiation. Analogous control experiments were performed either without Bi_2MoO_6 (blank) or with commercial Degussa P-25 TiO_2. Degradation was monitored by taking aliquots at given irradiation time intervals. The suspension including the photocatalyst and Rhodamine-B were centrifuged and the absorption spectra of the samples were recorded by measuring the absorbance at 553 nm with the UV–visible (Shimadzu UV-vis 3010) spectrometer. The concentration of RhB was calculated using the Beer-Lambert law $A = ecl$, where A is the absorbance at λ_{max} of RhB, e is the molar absorptivity of RhB, and l is the sample cell length (1 cm). RhB degradation was expressed as C/C_0 versus vis-irradiation time, where C_0 was the initial concentration. Total organic carbon (TOC) was measured with a Tekmar Dohrmann Apollo 9000 TOC analyzer.

Results and discussions

Synthesis and formation mechanism of Bi_2MoO_6 samples

Figure 1 shows XRD patterns of Bi_2MoO_6 samples prepared at different hydrothermal temperatures for 24 h. No peak of any other phases or impurities was detected. All of the diffraction peaks shown can be indexed as an orthorhombic phase of Bi_2MoO_6 and match well with the reported data (JCPDS card No. 76-2388). In Fig. 1, expanded diffraction peaks obviously reveal the crystalline phase would be nanosized. The cell constants of Bi_2MoO_6 are calculated to be $a = 5.476$ Å, $b = 16.145$ Å, and $c = 5.472$ Å by virtue of the (h, k, l) of every peak, the value of interplanar distance provided by X-ray diffractometer, and the formula: $d = (h^2/a^2 + k^2/b^2 + l^2/c^2)^{-1/2}$ where (h, k, l) are the indices of crystallographic plane, d is

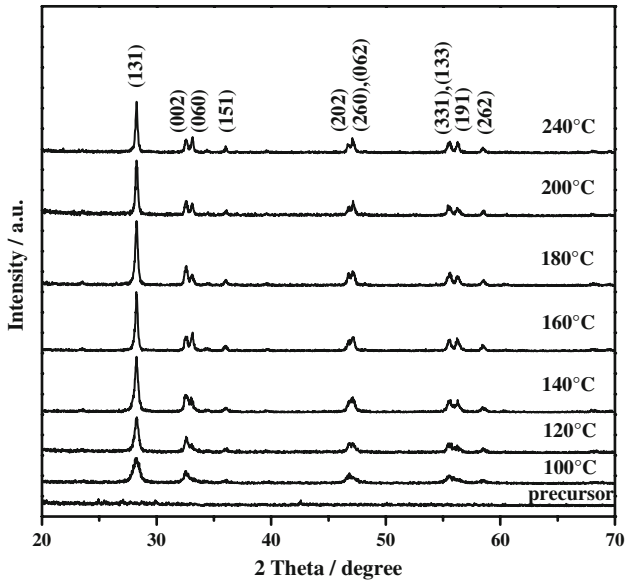

Fig. 1 X-ray diffraction patterns of the samples prepared by hydrothermal method at different temperatures for 24 h

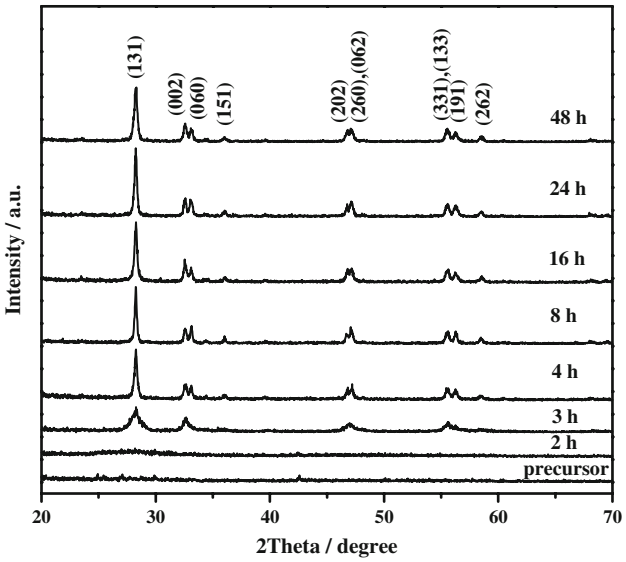

Fig. 2 X-ray diffraction patterns of the samples prepared by hydrothermal method at 180 °C for different times

the interplanar distance, (*a*, *b*, *c*) are the lattice parameters [26]. The XRD pattern of the starting precursor is also shown in Fig. 1. No diffraction peaks are observed. Amorphous precipitation occurs when NaOH solution is added to the mixture of $Bi(NO_3)_3$ and H_2MoO_4 before hydrothermal treatment. Therefore, the hydrothermal treatment is a prerequisite for the formation of crystalline Bi_2MoO_6 in the hydrothermal synthesis process. As shown in Fig. 1, temperature effect on the crystalline phase is demonstrated through the changes of the XRD patterns. When the temperature is increases from 100 °C to 180 °C, the shape of the diffraction peaks becomes more clear and the intensities increase gradually, which indicates the crystalline structure is improved. But when the temperature exceeds 180 °C, the intensity of the diffraction peak begins to decrease. By increasing the temperature to 240 °C, the intensity of the diffraction peak further decreases, indicating crystallinity becomes worse as estimated according to the well-known Scherrer equation.

Figure 2 shows the XRD patterns of the time series samples. When the temperature is settled at 180 °C, the diffraction peaks appears only after 3 h hydrothermal treatment. When the reaction time increases to more than 4 h, the XRD patterns clearly exhibit diffraction peaks of Bi_2MoO_6 crystal phases. It is obvious that the intensity of Bi_2MoO_6 peaks increase with treatment time. The optimum XRD pattern is obtained for 24 h of hydrothermal treatment. The longer or shorter reaction time leads to low diffraction intensities or worse XRD patterns.

Raman spectra of the samples synthesized by the different duration time at 180 °C are shown in Fig. 3. In general, Raman bands observed above 600 cm^{-1} for

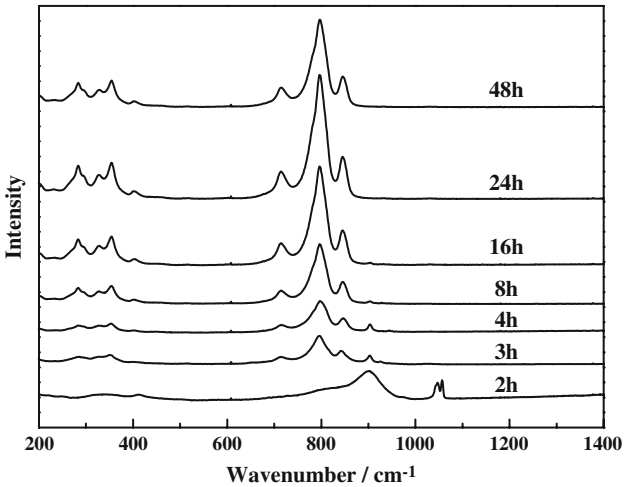

Fig. 3 Raman spectra of the as-prepared samples treated at 180 °C

Bi_2MoO_6 are assigned to Mo–O stretches and those below 400 cm^{-1} are assigned to bending, wagging and external modes by directly correlating the Mo–O bond lengths. The Raman spectrum of Bi_2MoO_6 phase shows a very strong band at 796 cm^{-1}, which is presumably A_{1g} mode, and represents the symmetric stretch of the MoO_6 octahedron. The bands with medium intensity at 713 cm^{-1} and 845 cm^{-1} also have A_{1g} character and are due to orthorhombic distortion of the octahedron. The modes between 270 and 360 cm^{-1} have E_g character, plausibly due to the rocking mode of the octahedron [14, 27, 28]. As can be seen in Fig. 3, the sample treated for 2 h exhibits characteristics of the precursor powders while the sample after 3 h treatment displays the specific band at 796 cm^{-1} of

Bi_2MoO_6. After 8 h treatment, the bands of the precursor almost completely disappear and Raman spectra exhibit the typical bands of Bi_2MoO_6. No significant shift in position can be observed in the Raman spectra of Bi_2MoO_6 with the increase of duration time after 2 h treatment. An increase in hydrothermal treatment time is connected with an increase in the intensities of the bands in the period of 3–24 h. The intensities of the peaks decrease as the hydrothermal treatment time further prolongs from 24 h to 48 h, suggesting a reduction of crystallite size. High crystallinity could be achieved above 8 h. These observations are in good agreement with XRD results.

To reveal the growth process of Bi_2MoO_6 particles, time-dependent experiments are carefully conducted and the samples are characterized by TEM. The morphologies of the as-prepared samples prepared at 180 °C for various hours are shown in Fig. 4. Figure 4a shows the TEM micrograph of the starting precursor, in which the morphology of this sample is nearly spherical colloids formed by agglomeration of nanoparticles. After 2 h hydrothermal reaction, the obtained product comprises smaller irregular particles in the range of several tens nanometers (Fig. 4b). The small particles are still amorphous. This result is consistent with the XRD result. When the reactants are hydrothermally treated for 3 h, some small laminar structure appeared among irregular particles (Fig. 4c). Small nanoplates formed and further grow at the cost of the small irregular nanoparticles. Finally the irregular nanoparticles almost disappear when treatment time further increases to 4 h. After that, the small nanoplates grow much bigger and exhibit an explicit edge. With an increase in the reaction time to 24 h, good-quality nanoplates could be obtained. The length of the edge could reach 400 nm. As shown in the inset of Fig. 4g, selective area electron diffraction (SAED) pattern of individual flat-lying nanoplates showed regular square diffraction spot array, revealing the single-crystal nature of the nanoplates. Further increase in the reaction time, the plate-like morphology could still be observed but these nanoplates show truncated corners or some breakage of the edges, making them have irregular outlines, as is shown in Fig. 4h for the 48 h sample.

Figure 5 shows SEM images of Bi_2MoO_6 samples prepared by the solid-state reaction (SSR, 550 °C, 5 h) and hydrothermal method at 180 °C for 24 h, respectively. The sintered products prepared by the solid-state reaction consisted of aggregates of particles with sizes of 100-400 nm. The sample prepared by hydrothermal method is platelike. The thickness of the nanoplates was about several nm and the average lengths are in extent of 200–400 nm. Thus the samples prepared by hydrothermal method have larger surface area compared to the SSR samples. It can also be concluded that hydrothermal synthesis can be carried out by a simple process and has been demonstrated as a versatile pathway toward shapes controlled nanocrystals. The wide range of operating temperatures available in aqueous media is the most attractive aspect of the approach. Moreover, the reaction parameters, such as the concentration of precursor, pH, synthesis temperature, and synthesis time are easily controlled.

On the basis of TEM observations, it can be concluded that the formation of Bi_2MoO_6 nanoplates is achieved via a typical Ostwald ripening process [29]. Under normal hydrothermal conditions, a highly supersaturated solution was adopted, and amorphous fine particles acted as the precursor for the synthesis of crystallized Bi_2MoO_6. At the beginning, when $Bi(NO_3)_3 \cdot 5H_2O$ and H_2WO_4 along with NaOH were added to deionized water, the irregular nanoparticles formed. Then the crystal growth followed. The larger particles grew at the cost of the small ones, due to the energy difference in solubility between the large particles and the smaller particles, according to the well-known Gibbs-Thomson law [30]. In early stages, an examination of the intermediate samples showed the coexistence of small laminar structure and irregular crystalline nuclei. As the reaction continued, irregular nanoparticles vanished and larger nanoplates formed. This suggested that the larger nanoplates grew at the cost of the smaller particles. It is well known that under the hydrothermal environment, nuclei could grow freely in aqueous solution (an open space) to form the nanocrystals with their natural habit, i.e., nanorods, nanoflowers, nanocubes, etc. Further crystal growth for the formation of 2D nanostructures was strongly related to the intrinsic crystal structure of Bi_2MoO_6. It has been reported that orthorhombic Bi_2MoO_6 is constructed by a corner-shared MoO_6 octahedral layer and $[Bi_2O_2]^{2+}$ atom layers sandwiched between MoO_6 octahedral layers. Peng [31] has shown that the shape of the nanostructures is strongly dependent on the relative chemical potential. It is believed that two-dimensional growth occurs only if the chemical potential of two surfaces is much higher than others. On the basis of Bi_2MoO_6 structure, the chains of octahedral-Mo equally exist along the *a*- and *c*-axes. The facets which are perpendicular to these chains usually have a much higher chemical potential in comparison with other facets. The above feature resulted in faster growth rates of these faces, and thus the crystal growth was preferentially along the layer. After 4 h of reaction, Bi_2MoO_6 nanoplates were attained. From this point of view, the hydrothermal method exhibits a particular advantage in the synthesis of nanostructured materials.

Band gap of the Bi_2MoO_6 nanoplates

UV–vis absorption measurement is one of the most important methods to reveal the energy structures and optical properties of semiconductor nanocrystals. Figure 6 shows

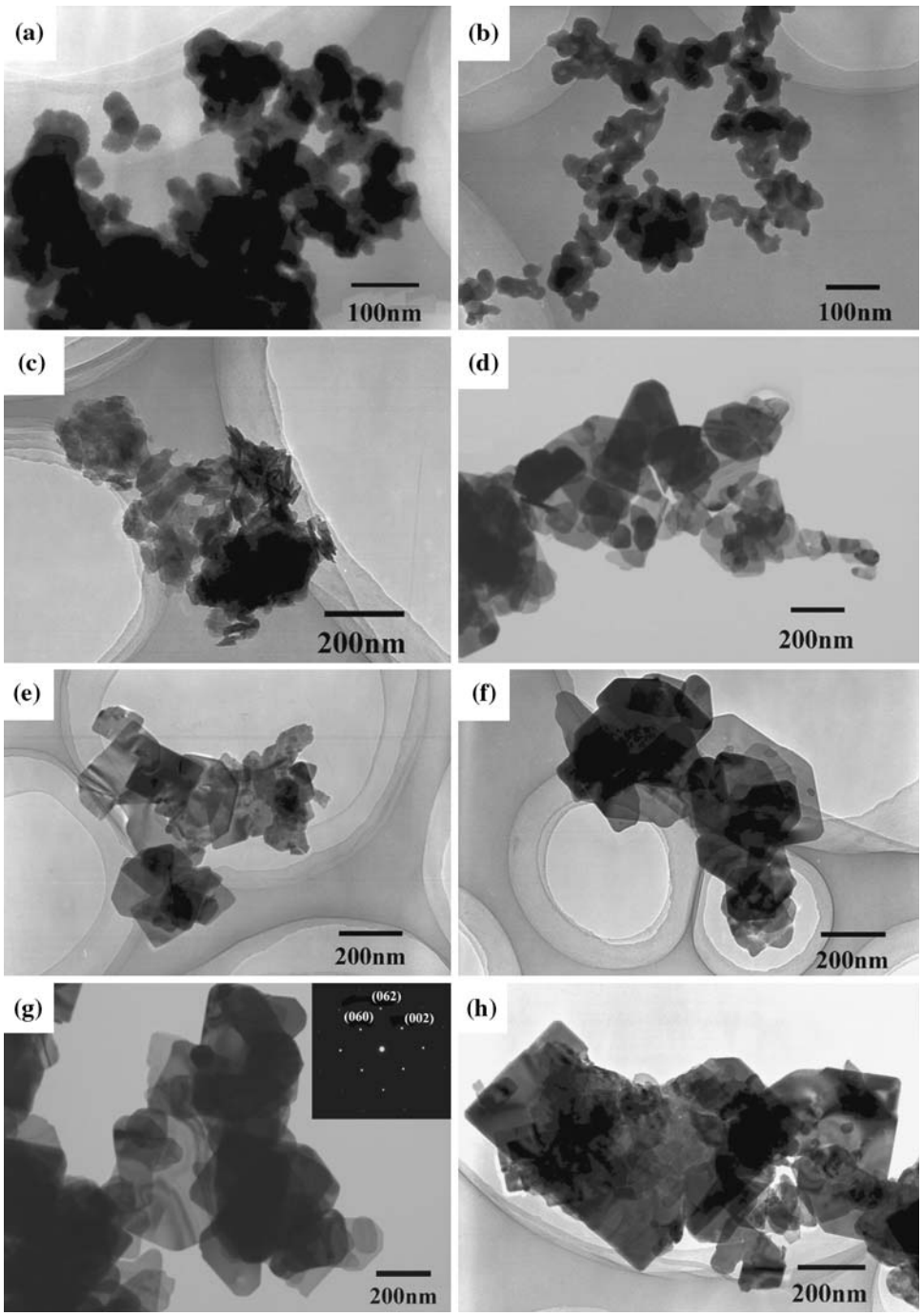

Fig. 4 TEM images of the samples synthesized at 180 °C for different hydrothermal times: **a** precursor, **b** 2, **c** 3, **d** 4, **e** 8, **f** 16, **g** 24, and **h** 48 h. The inset in (**g**) is the corresponding SAED pattern

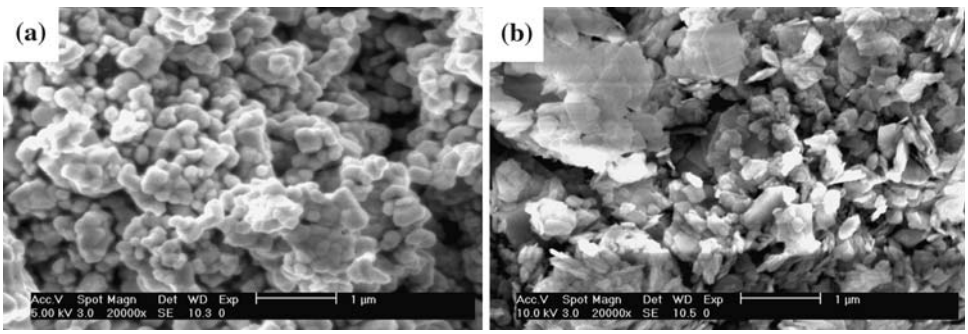

Fig. 5 SEM images of Bi_2MoO_6 the samples prepared by the solid-state (**a**) and hydrothermal methods (**b**)

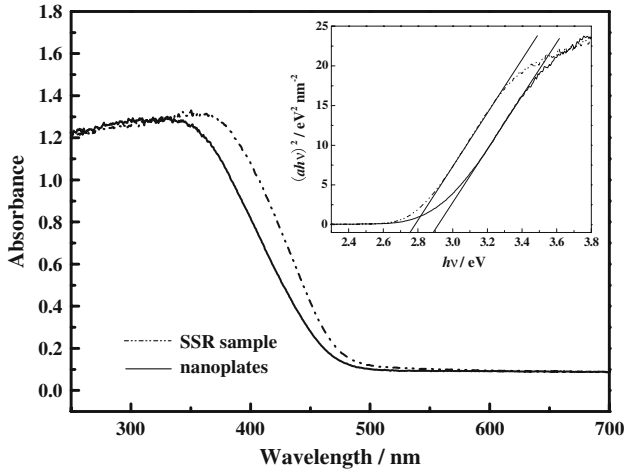

Fig. 6 UV–vis diffuse reflectance spectrum of as-prepared Bi_2MoO_6 nanoplates (180 °C for 24 h) and SSR sample. The inset is the $(ahv)^2$ versus hv curves

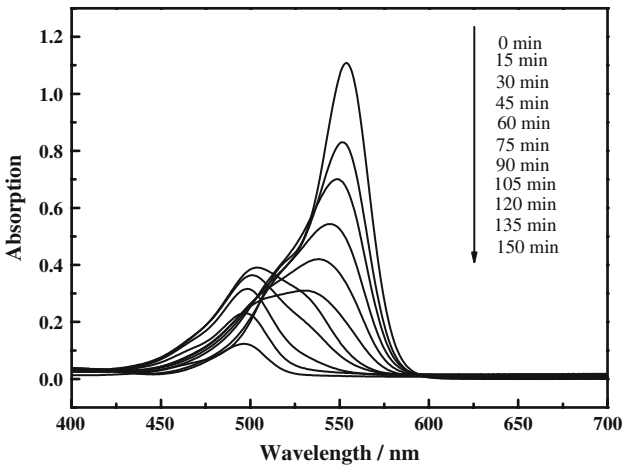

Fig. 7 UV–vis spectral changes of RhB in aqueous Bi_2MoO_6 (prepared at 180 °C, 24 h) suspensions

the UV–visible diffuse reflectance spectrum of hydrothermally prepared Bi_2MoO_6 powders (180 °C, 24 h) compared with the SSR sample (550 °C, 5 h). All optical absorption of the other hydrothermally synthesized Bi_2MoO_6 nanomaterials is nearly the same. It is showed that Bi_2MoO_6 presents the strong photoabsorption properties in the visible-light region around 470 nm. The steep shape of the spectra indicates that the visible-light absorption is not due to the transition from the impurity level but is due to the band-gap transition.

For a crystalline semiconductor, a classical Tauc approach is employed to estimate their optical energy band gaps using the following equation [32]

$$ahv = A(hv - E_g)^{n/2} \quad (1)$$

where a, v, E_g, and A are absorption coefficient, light frequency, band gap, and a constant, respectively. Among them, n decides the characteristics of the transition in a semiconductor. For a direct transition, n equals 1. Hence, the optical band gap for the absorption edge can be obtained by extrapolating the linear portion of the plot $(ahv)^2 - hv$ to $a = 0$. The results are shown in the inset of Fig. 6. The band gaps of the Bi_2MoO_6 nanoplates and SSR sample are estimated to be 2.88 and 2.75 eV, respectively. Compared with the bulk sample, the absorption of Bi_2MoO_6 nanoplates appears to blue-shift obviously, which might be interpreted by the nanosized effect [33]. The color of the nanoplates is light yellow, as can be expected from the absorption spectrum.

Photocatalytic activity

To study the photocatalytic activities of the hydrothermally prepared samples, tetraethylated rhodamine, RhB, with a major absorption band at 553 nm was chosen as a model organic pollutant. Figure 7 displays the temporal evolution of the spectra during the photodegradation of RhB photocatalysted by typical Bi_2MoO_6 nanoplates (180 °C, 24 h) under visible-light illumination. As shown in Fig. 7, in the photodegradation process, the absorption intensity decreased gradually and the major absorption band shifted from 553 to 496 nm step by step as the exposure time was extended, which is in good agreement with the previous reports [34, 35]. Under visible illumination, the blue-shift of the absorption band arises as RhB was de-ethylated in a stepwise manner. The fully *N*,*N*,*N*′,*N*′-tetraethylated rhodamine molecule (i.e., RhB) shows the major absorption band at 552 nm; *N*,*N*,*N*′-triethylated rhodamine, 539 nm; *N*,*N*′-diethylated rhodamine, 522 nm; *N*-ethylated rhodamine, 510 nm; and rhodamine, 498 nm [36, 37]. RhB formed rhodamine after being fully dethylated, and the rest was degraded through destruction of the conjugated structure. At the same time, the intense pink color of the starting RhB solution gradually faded. The absorption peaks corresponding to RhB completely disappeared after about 150 min, suggesting the excellent photocatalytic activity of the nanoplate sample.

Figures 8 and 9 display the degradation process of RhB using Bi_2MoO_6 samples prepared under different conditions as photocatalysts. For comparison, the RhB photodegradation by P-25 was also performed. It is clearly seen that the hydrothermal temperature and time have significant effects on the degradation rate of photocatalysts. Most of the samples exhibited higher photoactivity than P-25 under visible-light irradiation. Control experiments displayed that RhB did not degrade in Bi_2MoO_6 suspension in the dark or when illuminated with visible light at the absence of the catalyst. Therefore, the catalyst and visible light are indispensable to the RhB photodegradation. As shown in Fig. 8, the activities of catalysts increase with the rise of the treatment temperature

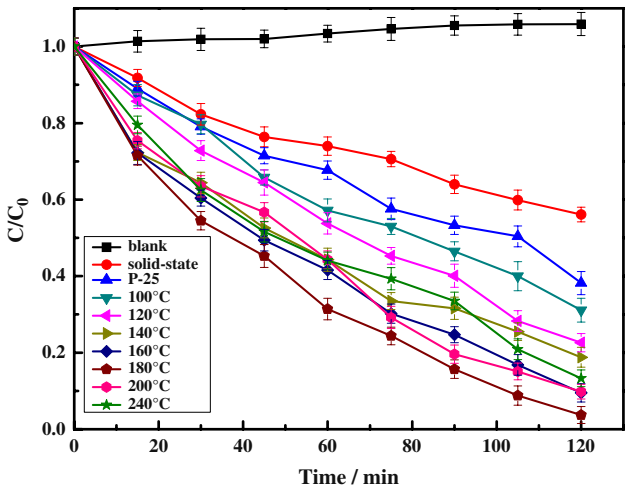

Fig. 8 Photocatalytic degradation of RhB over the samples prepared at different hydrothermal temperatures for 24 h under visible-light irradiation ($\lambda > 420$ nm); catalyst loading, 0.5 g L^{-1}; RhB, 1×10^{-5} M

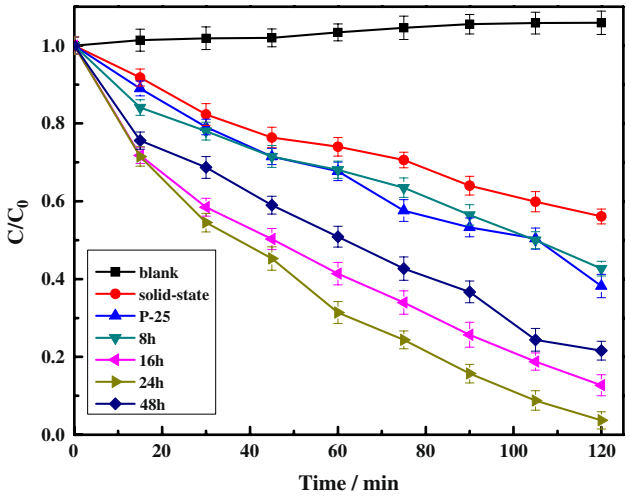

Fig. 9 Photocatalytic degradation of RhB over the samples prepared at 180 °C for different hydrothermal times under visible-light irradiation ($\lambda > 420$ nm); catalyst loading, 0.5 g L^{-1}; RhB, 1×10^{-5} M

before 180 °C. The sample prepared at 180 °C shows the highest photoactivity. The photodegradation rate reaches 96% within 120 min under visible-light irradiation. When the temperature further increased, the activities decreased. Figure 9 shows the effect of reaction time on the photocatalytic degradation of RhB when the temperature was settled at 180 °C. When the treatment time increased from 8 to 24 h, the RhB degradation rate increased. The highest activity was obtained at 24 h. Further prolonging the treatment time leads to the lower activity. This phenomenon is ascribed to the crystallinity of the as-prepared samples. As revealed in Figs. 1 and 2, the sample prepared at 180 °C, 24 h exhibits the best crystalline phase. The trend of photocatalytic activity is consistent with that of the crystallinity among temperature and time series. This indicates that the crystallinity is important factor that affects photocatalytic activity of the as-prepared sample. It is well known that lattice defects may act as recombination centers for the photoinduced electrons and holes, thus significantly reducing the net photocatalytic activity [38, 39]. The decrease in the photocatalytic activities of the samples prepared at other than 180 °C, 24 h may therefore be attributed to the increase of abundant lattice defects acting as inactivation centers due to their poor crystallinities, which could be observed from the XRD results.

The activities of the samples for all temperature series and time series after 8 h hydrothermal treatment are much higher than that of the corresponding sample prepared by solid-state reaction. This can be explained by their larger surface area and more capacious interspaces than the bulk material, which provide more active sites for the photocatalysts. At the same time, the thinness of the nanoplates results in a relatively large distortion of the unit cell due to the large surface strain, and the nanoplate structure means that electron–holes generated inside the crystal easily transfer to the surface and react with RhB. Therefore, Bi_2MoO_6 nanoplates display excellent photocatalytic activity because they not only have large surface area to increase the reaction place but also promote the efficiency of the electron–hole separation. The photocatalytic properties of Bi_2MoO_6 nanoplates should have significant technical applications in solar photocatalysis.

The extent of mineralization of dye is examined by determination of the total organic carbon (TOC) in the solution. The RhB decomposition and removal of TOC in the photocatalytic process are depicted in Fig. 10. Clearly, under visible-light irradiation, the rate of TOC reduction was slower than that of the degradation of RhB. When 96% of RhB were transformed after 120 min visible irradiation, about 21% of mineralized degree was reached. After irradiation for 5 h, about 72% of TOC was removed from the solution, which suggests the facile mineralization of RhB under visible irradiation. The decreasing rate of TOC exhibited two different behaviors before and after 120 min of irradiation, respectively, indicating that the mineralization of the dye goes through two different stages: de-ethylation in the initial photocatalytic degradation stage and the subsequent cleavage of the aromatic ring in the latter stage. As shown in Fig. 7, the hypsochromic shifts of the absorption maximum were rather significant. After irradiation for 120 min, the absorption band shifted from 553 to 496 nm. This evidence clearly indicated that de-ethylation predominated over the cleavage of the aromatic ring in the RhB dye. In this stage, TOC displayed a limited decrease, which indicates that mineralization of the dye molecules occurs only to a slight extent. On the other hand, in the latter stage, TOC of the solution decreased rapidly, indicating that the whole conjugated structure of RhB undergoes facile cleavage under visible irradiation.

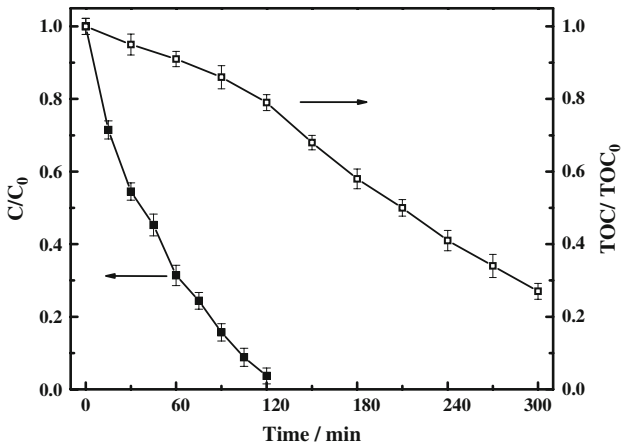

Fig. 10 Photocatalytic degradation and TOC removal of RhB over the Bi_2MoO_6 nanoplates (180 °C for 24 h) under visible-light irradiation ($\lambda > 420$ nm); catalyst loading, 0.5 g L^{-1}; RhB, 1 × 10^{-5} M

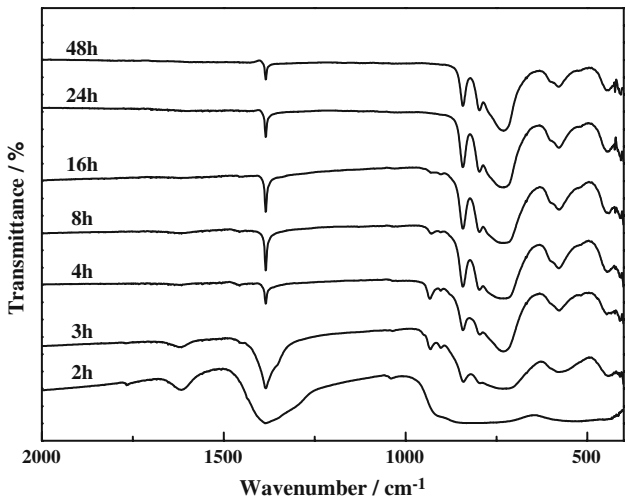

Fig. 11 FT-IR spectra of Bi_2MoO_6 prepared at 180 °C for different duration time

Figure 11 shows FT-IR spectra of Bi_2MoO_6 treated by different duration time. Two regions can be observed: one in the 950–700 cm^{-1} range, where the Mo–O stretching bands are recorded, and the other in the 600–400 cm^{-1} range, corresponds to stretching and deformation modes involving Bi–O modes [40–42]. The peaks of 1620 cm^{-1} and 1385 cm^{-1} in the IR spectra of the samples are assigned to the vibration of O–H. OH^- stretching vibration is sensitive to the change of the environment around the ion; therefore, OH^- absorption spectra can be used as a probe for defects [43–45]. Obviously, the absorption peak at about 731 cm^{-1} corresponding to Mo–O band becomes sharper, while the intensity of the peak at 1385 cm^{-1} becomes weaker with the increase of hydrothermal time except for 4 h. The peak at 1620 cm^{-1} almost completely disappears in the sample after 3 h treatment. These indicate that hydrogen-related defects in crystals decrease with the increase of hydrothermal time, which is in accord with XRD results (as shown in Fig. 2). At the same time, the removal of impurity groups could promote the rearrangement of the Mo–O network and the crystallization of Bi_2MoO_6. As discussed above, the improvement of crystallinity and decrease of defects may significantly enhance photocatalytic activity. Thus, photocatalytic activities of the time series samples increase with the treatment time.

Conclusions

In summary, Bi_2MoO_6 nanoplates were synthesized via a simple one-step hydrothermal route. The products during the hydrothermal process were characterized by XRD, SEM, TEM, Raman, and FT-IR spectroscopy. The effects of reaction temperature and time on the products were investigated. The nanoplates show a much higher photocatalytic activity than the bulk material for degradation of RhB under visible-light irradiation, suggesting potential future applications in photocatalysis by sunlight.

References

1. Fujishima A, Honda K (1972) Nature 238:37
2. Fujishima A, Rao TND, Tryk A (2000) J Photochem Photobiol C 1:1
3. Domen K, Kondo J, Hara M, Takata T (2000) Bull Chem Soc Jpn 73:1307
4. Kudo A (2007) Int J Hydrogen Energy 32:2673
5. Kudo A, Kato H, Tsuji I (2004) Chem Lett 33:1534
6. Kudo A (2003) Catal Surv Asia 7:31
7. Kendall KR, Navas C, Thomas JK, Zur Loye HC (1996) Chem Mater 8:642
8. Tsunoda Y, Shirata M, Sugimoto W, Liu Z, Terasaki O, Kuroda K, Sugahara Y (2001) Inorg Chem 40:5768
9. Kim JY, Chung I, Choy JH, Park GS (2001) Chem Mater 13:2759
10. Tsunoda Y, Sugimoto W, Sugahara Y (2003) Chem Mater 15:632
11. Buttrey D, Vogt T, White B (2000) J Solid State Chem 155:206
12. Ricote J, Pardo L, Castro A, Millan P (2001) J Solid State Chem 160:54
13. Sim LT, Lee CK, West AR (2002) J Mater Chem 12:17
14. Murugan R (2004) Phys B 352:227
15. Hartmanova M, Le M, Van Driessche I, Hoste S, Kundracik F (2005) Russ J Electrochem 41:455
16. Le M, Kovanda M, Myslik V, Vrnata M, Driessche I, Hoste S (2006) Thin Solid Films 497:284
17. Jung J, Kim H, Kim Y, Chung Y, Kim T, Lee S, Oh S, Song I (2007) Catalytic performance of bismuth molybdate catalysts in the oxidative dehydrogenation of C4 raffinate-3 to 1, 3-butadiene. Appl Catal A 317:244
18. Keulks GW, Rosynek MP, Daniel C (1971) Ind Eng Chem Prod Res Develop 10:138
19. Klisinska A, Mamede AS, Gaigneaux EM (2007) Catal Today 128:145

20. Yu J, Kudo A (2005) Chem Lett 34:1528
21. Shimodaira Y, Kato H, Kobayashi H, Kudo A (2006) J Phys Chem B 110:17790
22. Bi J, Wu L, Li J, Li Z, Wang X, Fu X (2007) Acta Mater 55:4699
23. Xie L, Ma J, Xu G (2008) Mater Sci Commun 110:197
24. Cruz A, Alfaro S, Cuéllar E, Méndez U (2007) Catal Today 129:194
25. Zhao X, Qu J, Liu H, Hu C (2007) Environ Sci Technol 41:6802
26. Niu X, Li H, Liu G (2005) J Mol Catal A 232:89
27. Hardcastle F, Wachs I (1991) J Phys Chem 95:10763
28. Graves P, Hua G, Myhra S, Thompson J (1995) J Solid State Chem 114:112
29. Yu SH, Liu B, Mo MS, Huang JH, Liu XM, Qian YT (2003) Adv Funct Mater 13:639
30. Mullin JW (1997) Crystallization, 3rd edn. Butterworth-Heinemann, Oxford, UK
31. Peng Z, Peng X (2002) J Am Chem Soc 124:3343
32. Butler M (1977) J Appl Phys 48:1914
33. Ball P, Garwin L (1992) Nature 355:761
34. Zhang C, Zhu Y (2005) Chem Mater 17:3537
35. Zhang L, Chen D, Jiao X (2006) J Phys Chem B 110:2668
36. Watanabe T, Takizawa T, Honda K (1977) J Phys Chem 81:1845
37. Inoue T, Watanabe T, Fujishima A, Honda K, Kohayakawa K (1977) J Electrochem Soc 124:719
38. Yoshino M, Kakihana M (2002) Chem Mater 14:3369
39. Zou Z, Ye J, Arakawa H (2002) J Phys Chem B 106:517
40. Carrazan S, Martin C, Rives V, Vidal R (1996) Spectrochim Acta A 52:1107
41. Trifiro F, Hoser H, Scarle R (1972) J Catal 25:12
42. Kovats W, Hill CG Jr (1986) Appl Spectrosc 40:1215
43. Xu T, Zhao X, Zhu Y (2006) J Phys Chem B 110:25825
44. Lin J, Lin J, Zhu Y (2007) Inorg Chem 46:8372
45. Li ZS, Yu T, Zou ZG, Ye JH (2006) Appl Phys Lett 88:071917